Feasibility of mapping radioactive minerals in high background radiation areas using remote sensing techniques

J.O. Ondieki [*], C.O. Mito, M.I. Kaniu

Department of Physics, University of Nairobi, P. O. Box 30197-00100, Nairobi, Kenya

ABSTRACT

This study investigates the utility of using remote sensing and geographic information system techniques to accurately infer the presence of radioactive minerals in a typical high background radiation area (HBRA) by analyzing spectral signatures of associated soil, rocks and vegetation. To accomplish this, both unsupervised (K-Means Clustering) and supervised classification techniques based on a maximum likelihood classifier (MLC) were applied to Landsat-8 Imager data from Mrima Hill on Kenya's south coast. The hill is surrounded by dense tropical forest and deeply weathered soils which are rich in Nb, Th, and rare earth elements. Due to high activity concentrations of ^{232}Th (>8 times higher than the world average value for soil), the hill has been designated as a geogenic HBRA. Based on the underlying geological formations, four classifications of vegetation and two classifications of soil/rocks were established and used to indicate the presence of radioactive minerals in the area. Measurements of air-absorbed gamma dose-rates in the area were successfully used to validate these findings. The application of the MLC method on Landsat satellite data shows that this method can be used as a powerful tool to explore and improve radioactive minerals mapping in HBRAs, the overall classification accuracy of Landsat8 OLI data using botanical technique is 80% and the Kappa Coefficient is 0.6. The overall classification accuracy using soil/rocks spectral signatures is 91% and the Kappa Coefficient is 0.7. Finally, the study demonstrated the general utility of remote sensing techniques in radioactive mineral surveys as well as environmental radiological assessments, particularly in resource-constrained settings.

1. Introduction

Carbonatites and alkaline intrusive complexes are examples of high background radiation areas (HBRAs). This is due to the abundance of rare earth elements (REEs) and heavy elements such as Nb, Zr, and Mn, which are often associated with thorium and uranium -bearing minerals like monazite and pyrochlore (Verplanck and Gosen, 2011). Because these minerals contain anomalous concentrations of natural radionuclides, mining waste generated during mineral processing activities can be highly radioactive, posing a risk to human health and environment. Geophysical techniques such as radiometric, magnetic, and gravity have been widely used to analyze such intrusions (Killeen et al., 2015; Thomas et al., 2016), but due to the large number of samples required for analysis, they are time consuming and expensive, making them unsuitable for laboratories with limited resources. Remote sensing techniques, on the other hand, are preferred in geological applications (Rajesh, 2004; Rokos et al., 2000) due to their low cost and ability to access difficult terrains and landforms (e.g., mountainous and forest terrains). Furthermore, large-scale data collection may be done quickly and at regular intervals (Rajan Girija and Mayappan, 2019; Samanga, 2021).

Although both the hyperspectral (HS) and multispectral (MS) sensors are employed in mineral mapping, HS are more sensitive to variations in reflected energy than MS due to their superior spectral resolution and offer a greater potential for identifying a range of minerals. Previous studies (Boesche et al., 2015; Neave et al., 2016; Turner et al., 2014) have widely and successfully used HS data to map REE-bearing minerals. ASTER and Landsat are the most widely used MS data for mineral mapping, but due to their low spectral resolution, they are rarely used in the mapping of REE-bearing and radioactive minerals (Rowan and Mars, 2003). Nonetheless, MS sensors are useful, particularly in exposed bedrock areas (Leverington and Moon, 2012). As a result, the Landsat Thematic Mapper (TM) and Landsat Enhanced Thematic Mapper Plus (ETM+) satellites have been used to differentiate between different lithologies (Amer et al., 2012; Crosta et al., 2003; Ramadan and El Leithy, 2005).

Several methodologies have been used to analyze MS data, including principal component analysis (PCA) (Yang et al., 2008), band ratios
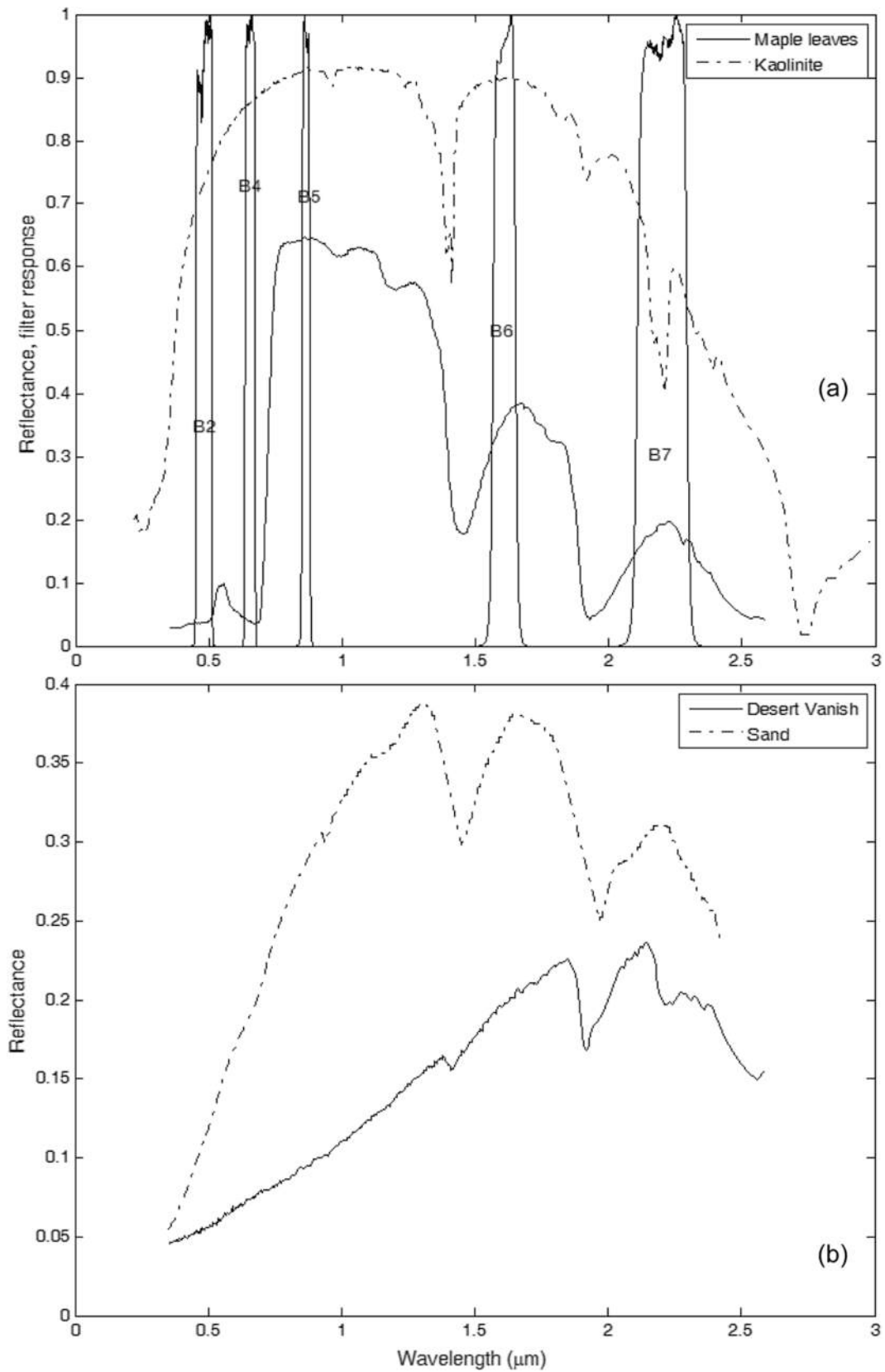
Fig. 1. (a) Reflectance of vegetation (Maple leaves) and mineral (Kaolinite) and filter response of Landsat OLI bands, and (b) Reflectance of rock (Desert Vanish) and soil (Sand).
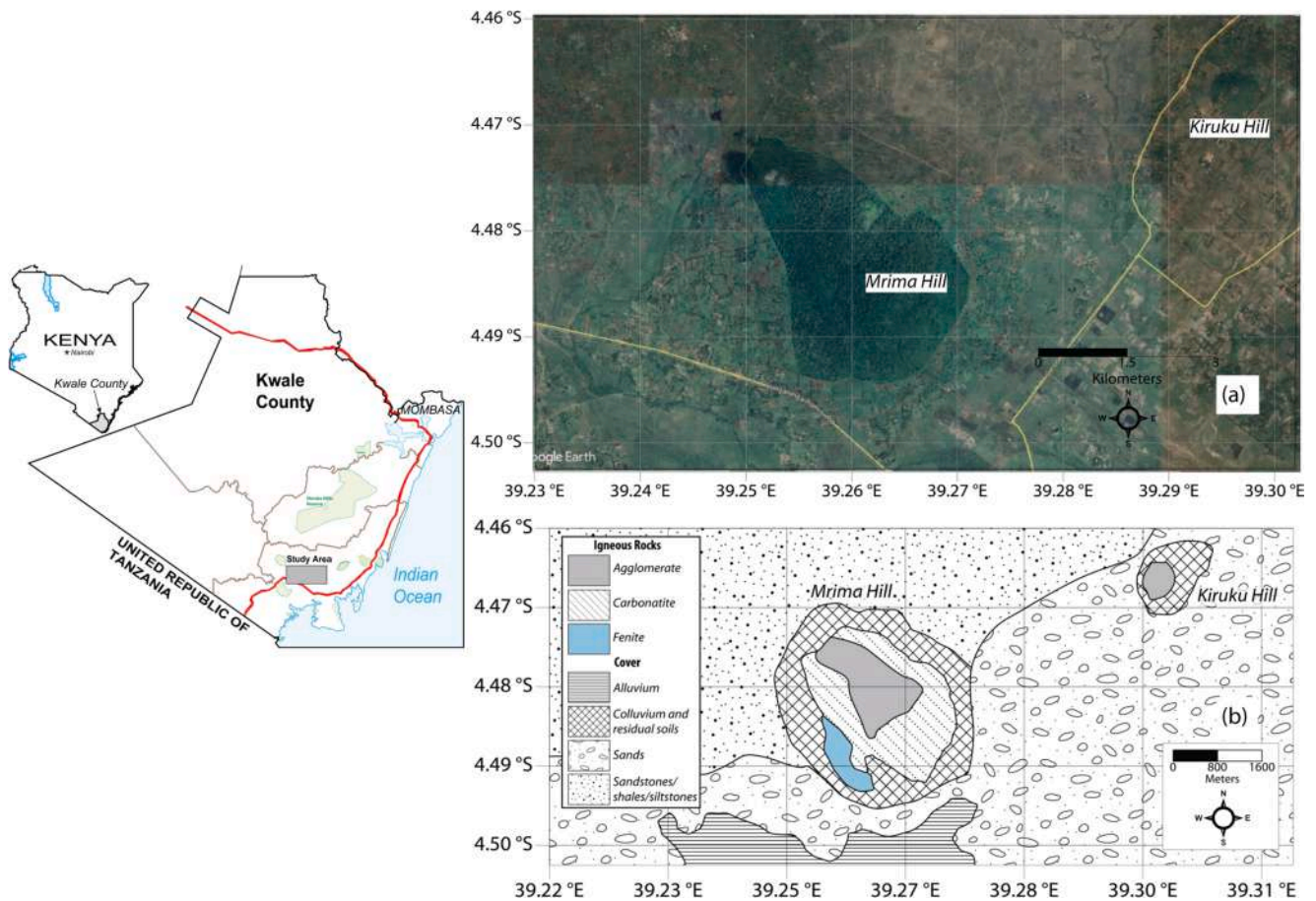
Fig. 2. (a) Satellite imagery of the study area (source: Google Earth) and (b) Map indicating geology of the study area (Adapted from: JICA, 1993).

(Rowan and Mars, 2003), relative absorption band depth (Crowley et al., 1989), mineral indices (Abrams and Yamaguchi, 2019), as well as spectral analysis (Pacheco and McNairn, 2010). Band ratios have been employed to investigate spectral differences between bands and to reduce topographic effects. Despite the improvement in image contrast, its weakness is demonstrated by the reduction in the reflection intensity of objects on the images. Also, there could be more than one mineral candidate for the same band ratio e.g. Landsat band ratio of 4/2 and 4/1 both used for discriminating iron minerals and ferrous minerals. Furthermore, although the PCA technique helps in identifying minerals, it is not definitive in discriminating or naming the various possible minerals which may constitute the brighter color exhibited by a particular group of pixels at a specific location on the image.

The maximum likelihood classification method, on the other hand, is widely used and can be regarded as one of the most reliable techniques for feature identification in remote sensing. For this reason we propose to use it in this work. It is a parametric statistical method in which the analyst supervises the classification by identifying representative areas known as training zones. These zones are then described numerically and presented to the computer algorithm, which classifies the pixels of the entire scene into the respective spectral class that appears to be most alike. It is assumed that the training data distribution is Gaussian (normally distributed). The probability density functions are used to classify a pixel by computing the likelihood of the pixel belonging to each class. During classification all unclassified pixels are assigned class membership based on the relative likelihood of the pixel occurring within each class probability density function (Lillesand et al., 2015). It is therefore, a statistical decision criterion to assist in the classification of overlapping signatures; pixels are assigned to the class of highest probability.

To validate their findings, most studies that use remote sensing

techniques to map radioactive minerals have relied primarily on field samples and laboratory analysis techniques (Manuel et al., 2017; Mohamed et al., 2021; Muavhi et al., 2021; Ramadan et al., 2013; Shi et al., 2020). These usually necessitate extensive planning as well as deployment of manpower and resources on the ground thus limiting the number of samples collected. Airborne radiometric measurements (Baranwal and Rønning, 2020) would be the most cost-effective approach for large-scale surveys, but the systems are expensive and not available in most laboratories. GPS equipped detectors for vehicular and mobile backpack γ-ray spectrometry (Aage et al., 2006; Kaniu et al., 2018a) can be useful for laboratories with limited resources in the establishment of baseline radiological maps that include a spatially representative dataset for validation. In this paper, we investigate the feasibility of remote sensing techniques in mapping radioactive minerals in a typical HBRA. We show how the maximum likelihood supervised classification technique can be used to map soil/rocks and vegetation species associated with radioactive minerals based on their spectral response to electromagnetic radiation. We also demonstrate how *in-situ* air absorbed gamma dose rate measurements can be used to validate the classified data.

2. Interactions of electromagnetic radiation with vegetation, rocks, soil and minerals

Rocks are mineral aggregations that contain a wide range of molecules and elements such as silicon, aluminum, iron and calcium. The spectral reflectance of various minerals can thus be used to identify minerals and consequently rocks using remotely sensed data (Mather and Koch, 2010). For example, spectral band rationing enhances compositional information while suppressing other types of information
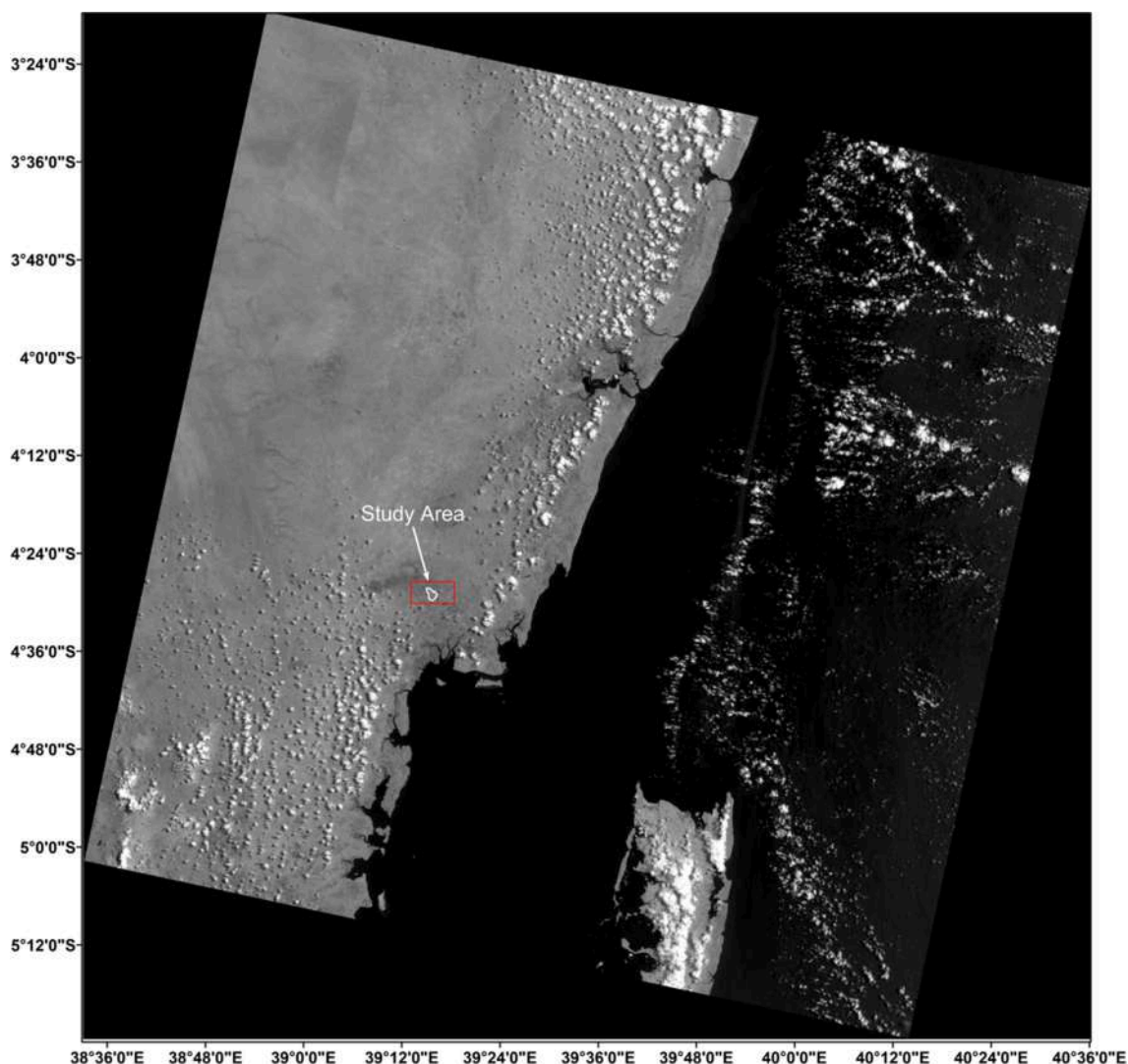
Fig. 3. Raw Landsat-8 (Path 166/Row 63) of the study area acquired on 30th March 2016, 07:31:17.

about earth's surface. Fig. 1 shows the spectral reflectance curves of some common vegetation (Maple), mineral (Kaolinite), rock (Desert Vanish) and soil (Sand) found on the earth's surface and filter response of Landsat 8 OLI bands.

This method is very useful for highlighting certain features or materials that cannot be seen in the raw bands. The ratio of bands 4 and 5 is useful for vegetation mapping by using the Normalized Difference Vegetation Index (NDVI). Band ratio transformation is useful for qualitative detection of hydrothermal alteration minerals (Di Tommaso. 2007; Rockwell et al. 2008; Pour and Hashim. 2011). The ratio 4/2 is useful for mapping iron oxides because it has absorption in the blue region, while it has a high reflectance in the red region. The ratio 6/7 can be used to map kaolinite, montmorillonite and clay minerals. All these features have a high reflectance in band 6 and low reflectance in band 7 of Landsat 8 image. The ratio 6/5 is useful in mapping ferrous minerals due to the high reflectance of these minerals in these bands. Two combinations of RGB images can been used for lithological mapping and hydrothermal alteration zones i.e., the ratios 4/2, 6/7 and band 6/5 as RGB and 4/2, 6/5 and 6/7 as RGB (Sabins, 1999). Identification of iron oxides can be implemented using bands 2 and 4 while mapping of clay and carbonate minerals is carried out using bands 6 and 7 of Landsat-8. Band ratios derived from image spectra (4/2, 6/7, 5/4 in RGB) are useful in the identification of rock units alteration.

3. Materials and methods

3.1. Description of the study area

Mrima Hill is located on Kenya's south coast, around 80 km southwest of harbor city of Mombasa. The area is defined between latitudes 4° 27 and 4° 30 and longitudes 39° 13 and 39° 18. The hill is dome-shaped and is covered by a dense tropical forest (see Fig. 2(a)). It rises roughly 300 m above sea level and covers an area of around 3.8 km^2. The presence of *Dovyalis keniensis*, an 18-species genus that includes *Asparagus* sp, as well as plants such as sagebrush, pynon pine and mormon tea vegetation all of which are used in depicting radioactive materials, has been previously recorded in the area (Gillman, 1949; Sleumer et al., 1975). In addition, the hill is a carbonatite plug of Jombo's alkaline igneous complex (Baker, 1953; JICA, 1993), and it contains Duruma deposits as well as alkaline, igneous, and sedimentary rocks (see Fig. 2 (b)). Fe, Mn, and REEs as well as U and Th-bearing minerals are also abundant in the area. Recently, Kaniu et al. (2018a, 2018b) found that the air absorbed gamma dose-rates in the area ranged from 60 to 2368 nGy h^{-1}, with the higher dose-rates (>600 nGy h^{-1}) in the hill crest correlating with elevated ^{232}Th activity concentrations.

3.2. Remote sensing data

Landsat-8 (Path 166/Row 63) operational land imager (OLI) and thermal infrared sensor (TIRS) data were downloaded in a digital format with 16-bit pixel values characteristics from the United States Geological Survey (USGS) website on March 30, 2016. There are a total of 11 bands. Bands 2, 3, 4, 5, 6, and 7 were processed and merged with a 30 m resolution. The technological parameters of Landsat-8 remote sensing sensors are as described by Dev Acharya et al., (2015). The satellite data resolution, path/row, and acquisition date are all as shown in Fig. 3. The scene was cloud-free and georeferenced to the WGS-84 datum using the UTM zone 36 south projections.

3.3. Satellite image preprocessing

Satellite sensor data typically contains unique radiometric and geometric errors, necessitating rectification. Due to differences in scene illumination and viewing geometry, atmospheric correction, and sensor noise, radiometric correction will be required. For atmospheric adjustments, the relative normalization and absolute normalization (Adelman-McCarthy et al., 2006) as well as absolute rectification (Chavez, 1996; Song and Woodcock, 2003) methods are used. Fast Line-of-sight Atmospheric Analysis of Hypercubes (FLAASH) module in ENVI software was used in this study to alter the atmosphere using an atmospheric code based on MODTRAN 4 radiative transfer.

The interpretation of multi spectral remote sensing images for geological purposes is hampered by vegetation cover, particularly in highly covered landscapes. To increase the underlying geological information in such terrains, it is preferable to lower the reflectance component of vegetation. The vegetation reflectance component in the research area was suppressed using the forced invariance approach (Yu et al., 2011). The procedure is divided into three steps, as follows: (1) the suppression of sparsely vegetated or non-vegetated areas using Normalized Difference Vegetation Index (NDVI); (ii) the combination of the vegetated and non-vegetated areas followed by histogram equalization to eliminate color saturation differences; and (iii) the use of forced invariance technique in subtracting the spectral response in relation to vegetation. NDVI was utilized in this investigation, given by (near-infrared -red)/(near-infrared + red) and has values ranging from −1 to 1. The non-vegetated areas were retained by concealing the areas with NDVI less than 0.25. Non-vegetated portions were separated and masked before being added using maskings-adding technique.

3.4. Image classification

To capture the spectral variability of the study area, we used an unsupervised classification procedure [(ENVI version 5.3) (K-Means Clustering algorithm)] on a 2016 Landsat OLI scene of the study area (30 March, centred on Path 166 and Row 63) to identify 4 and 2 spectral classes for vegetation and soil/rocks, respectively. In K-Means clustering: 1. a set number of cluster centres are positioned randomly through the spectral space; 2. pixels are assigned to their nearest cluster; 3. the mean location is re-calculated for each cluster; 4. Steps 2 and 3 repeated until movement of cluster centres is below threshold and then assign class types to spectral clusters. Use of additional classes might have captured more of the spectral variability in the image; however, we believed that the 4 and 2 classes sampled a reasonable spectral range according to the existing knowledge of the study area.

We then used a supervised (MLC) method to classify satellite images into vegetation and soil/rocks. Assumptions of supervised methods are that (1) a continuum of ground characteristics (e.g., present ground cover of vegetation and soil/rocks) meaningful to the study can be divided into discrete categories (e.g, vegetation and soil/rock classes), and (2) those categories can be mapped from satellite data. Supervised classification needs the background knowledge of study area obtained by external sources or field work. The training fields are used to train the
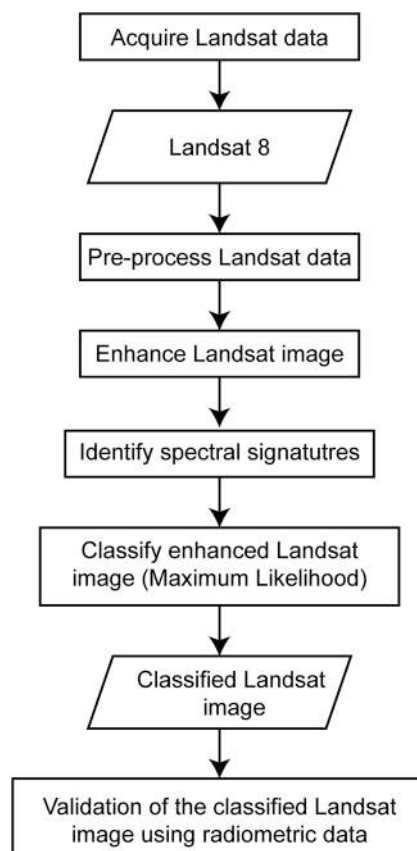

Fig. 4. Schematic representation of overall analysis steps for mapping radioactive minerals.

computer in recognizing different categories. The selection of training fields is based on optical properties of each category, field observations at known locations, and ariel and ground photographs. When the interpreter enters a single pixel, the algorithm adds up the neighbor pixels with identical pixel values to the one that was initially entered.

We do emphasize mapping of radioactive minerals by inferring to vegetation and soil/rocks spectral classes and air absorbed gamma dose-rates relationships in our research and not by specific vegetation or rock/soil species. This is due to limited plant/rock/soil species and hyperspectral data of the study area. We therefore, developed a classification to reflect vegetation and soil/rock classes that are correlated with dose-rates, abundance, and distribution.

We used a per-pixel approach in this study. Vegetation and soil rock sampling and classification were scaled relative to an OLI pixel size, and image classification and accuracy assessment were conducted on a per-pixel basis.

The soil/rocks and vegetation were classified into different classes based on the spectral distance between the closest pixels. The remote sensing image of the study area was classified using the Region of Interest (ROI) of the spectral signatures of the vegetation, soil/rocks types available in the ENVI 5.3 software spectral library database. For best input, the ENVI interface module's high probability threshold for each class was set at 0.9 for soil/rocks and 0.8 for vegetation species identified in the study area. To obtain the best results, the probabilities were estimated by altering the input values between 0.1 and 1.0.

3.5. Validation of classification data

Air absorbed gamma dose-rate measurements in the study area were obtained in 2014 and 2019 with a portable PGIS-2 *in-situ* -ray spectrometer and the Safecast bGeigie Nano radiation detector, respectively.
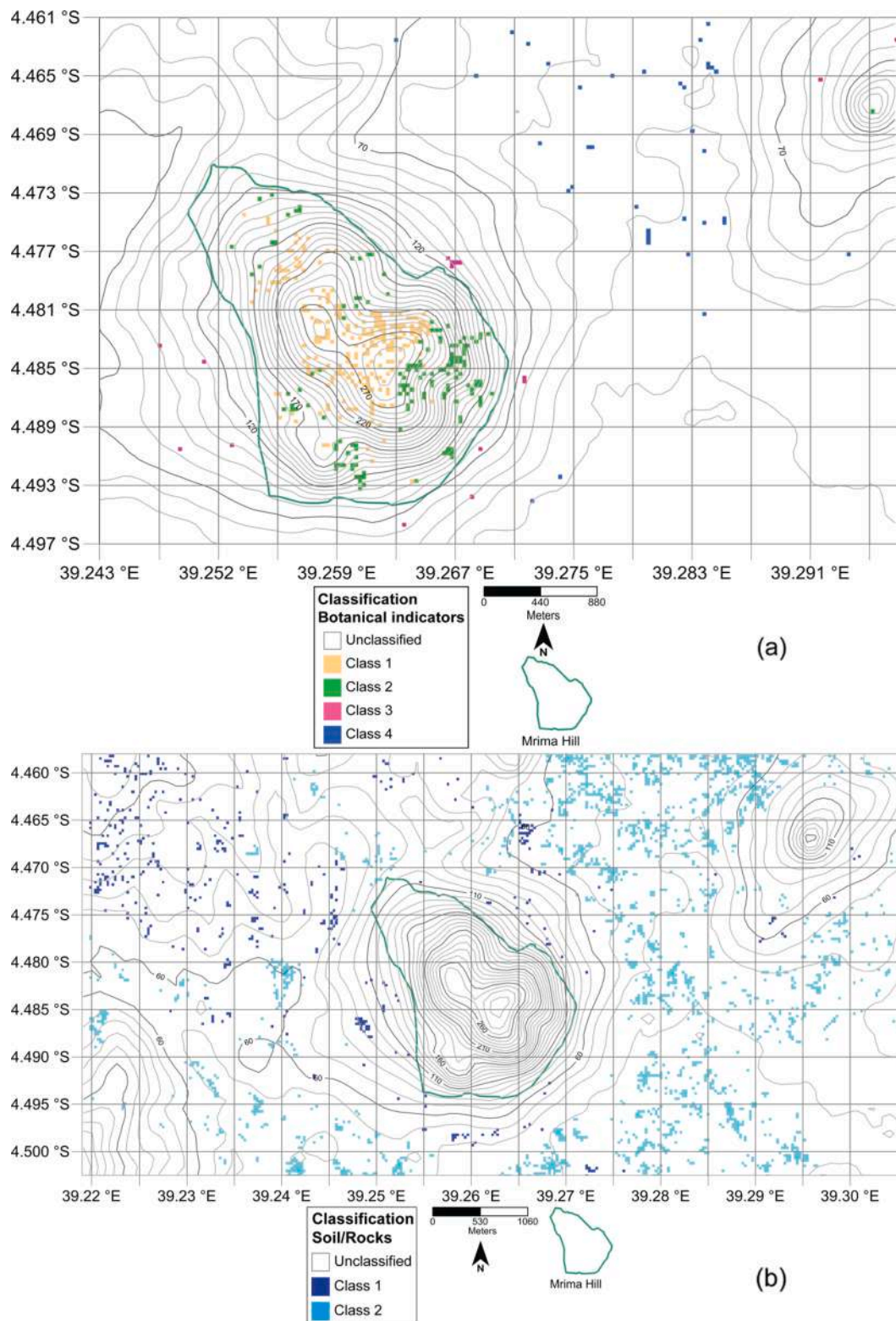
Fig. 5. Maximum likelihood classification of (a) vegetation species in Mrima Hill and (b) soil/rocks in the Mrima Hill environs.

The techniques employed, as well as a thorough description of how these measurements were collected, can be found elsewhere (Kaniu et al., 2018a, 2019). These measurements were used to validate the maximum likelihood classification data. The Surfer13 (Golden Software, LLC) software was used to superimpose the geo-referenced radiometric data on the classification data. To quantitatively evaluate the accuracy of the classification data, a pixel-by-pixel comparison was used to calculate a confusion matrix about the agreement between the classified results and the dose-rate measurements. The overall steps involved in mapping the radioactive materials in the study area can be summarized using the six steps described in Fig. 4.

Table 1
Binning scheme for air absorbed gamma dose-rates in the study area.

Area	Dose rate range (nGy h^{-1})	%	Description
Mrima Hill No. measurements: 17,452 Background: 651 ± 436 nGy h^{-1}	41–215	10	Below the Mrima Hill background value
	215–1087	77	Within the Mrima Hill background value
	1087–3971	13	Higher than the Mrima Hill background value (gamma radiation hotspots)
Mrima Hill environs No. measurements: 3922 Background: 223 ± 144 nGy h^{-1}	40–79	18	Below the Mrima Hill environs background value
	79–367	68	Within the Mrima Hill environs background value
	367–967	14	Higher than the Mrima Hill environs background value (gamma radiation hotspots)

4. Results and discussion

4.1. Image classification

Because Mrima Hill is covered by dense forest and thick undergrowth (see in Fig. 2(a)), no soil/rock signatures were obtained. Instead, by evaluating the spectral signatures of associated vegetation, the botanical technique was utilized to infer the existence of radioactive materials in the area. The vegetation species were classified into Class 1, Class 2, Class 3 and Class 4 by the use of maximum likelihood classifier, see Fig. 5 (a). It was found that the hill summit has more signatures than the surrounding areas. Class 1 vegetation species are more concentrated on

the hill peaks than Class 2 vegetation species, which are more concentrated on the upper slopes. Class 3 vegetation species are concentrated on the lower slopes around the hill whereas Class 4 vegetation species are sparsely distributed about 0.5–3 km away from the hill. It was also noted that the population of Class 3 vegetation species is lower than the other species. Fig. 5(b) shows that the two types of soil/rocks in the areas surrounding Mrima Hill had a high probability of being classified because the area is not covered by vegetation. The distribution of Class 1 soil/rocks is concentrated in the north-west areas and around the hill, whereas Class 2 soil/rocks are mostly found in the eastern and southern part of the Mrima environs.

4.2. Validation of the classification results

Table 1 summarizes the binning method used, as well as statistics for the gamma dose-rate absorbed by the air measurements used to validate the maximum likelihood classification results. In general, measurements in both Mrima Hill (>90%) and Mrima Environs (>82%) are 3.6–66.2 and 1.3–16.1 times, respectively higher than the population-weighted world average external background radiation rate of 60 nGy h^{-1} (UNSCEAR, 2000). The background values for both Mrima Hill and the environs were estimated as 651 ± 436 nGy h^{-1} and 223 ± 144 nGy h^{-1}, respectively.

The comparison of Mrima Hill classification data with air absorbed dose-rates (Fig. 6) shows that most of the above background dose-rates (hotspots), i.e. >1018 nGy h^{-1} can be associated with Class 1 vegetation (see grids F2, G1, G2 and H3). Background dose-rates i.e. 215–1018 nGy h^{-1} can be associated mostly with Class 2 and Class 3 vegetation (see grids E4, F4, G4 and H2). Class 4 vegetation can be associated with below background dose-rates i.e. 41–215 nGy h^{-1} (see grids A1, A2, A3, D3 and D4). Table 2 shows the confusion matrix derived from the
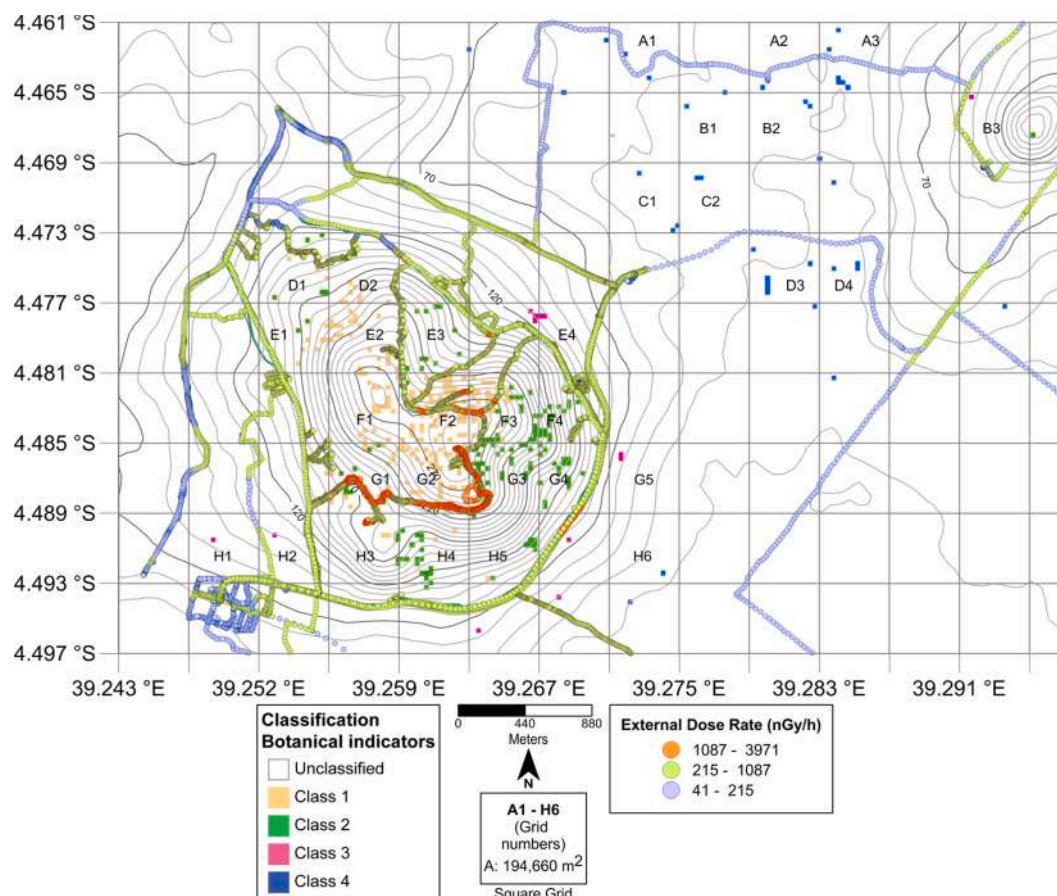

Fig. 6. Maximum likelihood classified data for Mrima Hill overlaid with air-absorbed gamma dose-rates.

Table 2

Confusion matrix between maximum likelihood classification and air absorbed gamma dose-rates in Mrima Hill.

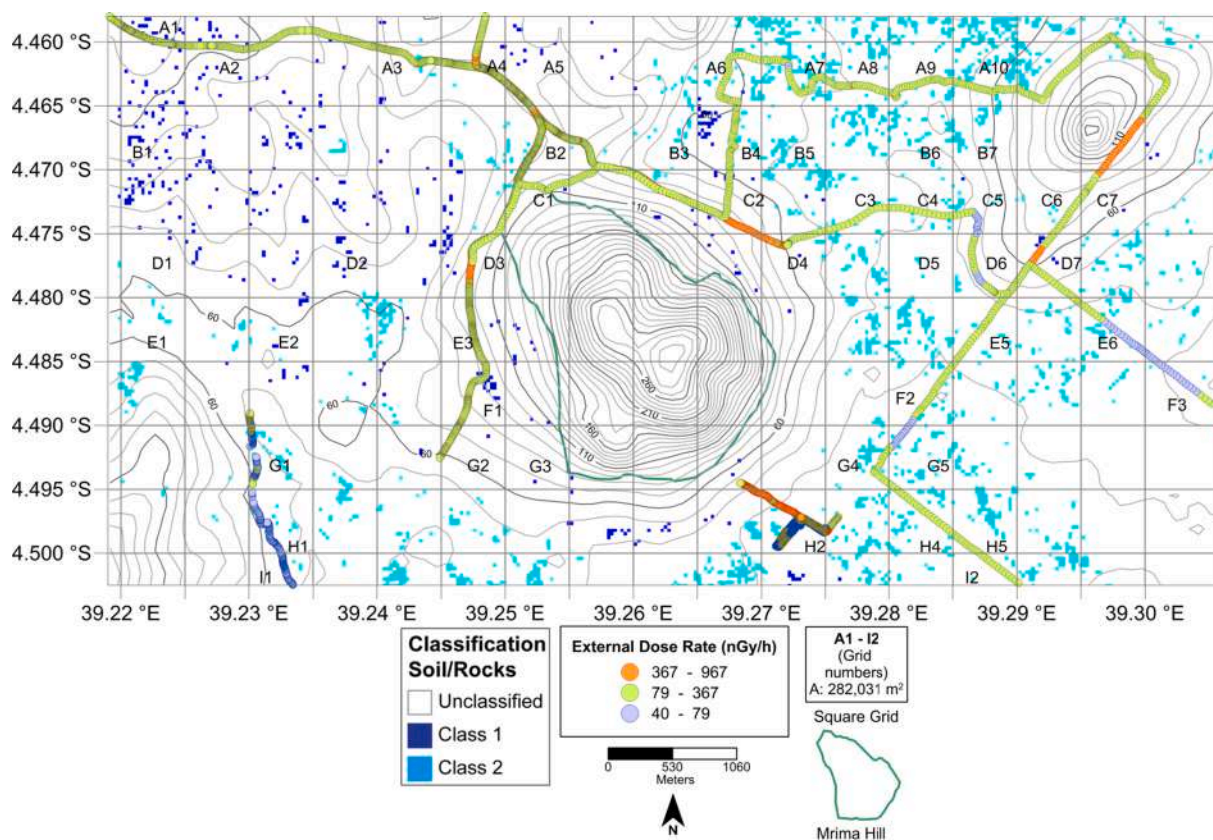| Item		Training data				
		Class 1 (719–3658 nGy h^{-1})	Class 2 (375–679 nGy h^{-1})	Class 3 (284–363 nGy h^{-1})	Class 4 (77–154 nGy h^{-1})	Total
Maximum likelihood classification results	Class 1 (719–3658 nGy h^{-1})	160	35	–	–	195
	Class 2 (375–679 nGy h^{-1})	14	68	–	–	82
	Class 3 (284–363 nGy h^{-1})	10	4	4	–	18
	Class 4 (77–154 nGy h^{-1})	–	–	1	18	19
	Total	184	107	5	18	314
Overall accuracy		80%				
Kappa coefficient		0.62				

Fig. 7. Maximum likelihood classified data for Mrima Hill environs overlaid with air-absorbed gamma dose-rates.

Table 3

Confusion matrix between maximum likelihood classification and air absorbed gamma dose-rates in the Mrima Hill environs.

Item		Training data		
		Class 1 (162–686 nGy h^{-1})	Class 2 (92–131 nGy h^{-1})	Total
Classification results	Class 1 (162–686 nGy h^{-1})	103	34	137
	Class 2 (92–131 nGy h^{-1})	33	632	665
	Total	136	666	802
Overall accuracy, Kappa coefficient:		91%, 0.7		

classified data and the air absorbed gamma dose-rate measurements in the indicated grids (Fig. 6). It was found that the overall classification accuracy is 80% and the kappa coefficient is 0.6.

Mrima Hill and its environs cover a total area of ≈ 29 km^2, and due to the limited resources and man-power, only a few areas of the environs were accessed during the radiological surveys. Despite this, there were enough measurement points to compare to the maximum likelihood classification data (see Fig. 7). It was observed that Class 1 soil/rocks were found to correspond with background dose-rates measurements and hotspots i.e. >79–967 nGy h^{-1}), see for example grids A1, A4, C2, D3 and D. Class 2 soil/rocks can be associated with both below background and background dose rate measurements, i.e. 41–<367 nGy h^{-1}; see for example grids A6, A7, A8, A9, G1, G5 and H1. Table 3 shows the confusion matrix derived from the classified data and the air absorbed gamma dose-rate measurements in the indicated grids (Fig. 7). It was found that the overall classification accuracy is 91% and the

Table 4
Projected air absorbed gamma dose-rates based on maximum likelihood classification data.

Fig/Grid No.	Maximum Likelihood Classification	Projected gamma dose-rates (nGy h^{-1})
Fig. 6: E1, F1	Class 1 (vegetation)	719–3658
Fig. 6: E3, H4, H5, H1	Class 2 (vegetation)	375–679
	Class 3 (vegetation)	284–363
Fig. 6: H1, G5	Class 4 (vegetation)	77–154
Fig. 6: B1, B2, C1, C2, H6		
Fig. 7: A2, A5, B1, D2, E2	Class 1 (soil/rocks)	162–686
	Class 2 (soil/rocks)	92–131
Fig. 7: B5, B6, B7, E1, E5		

kappa coefficient is 0.7.

4.3. Discussion

The dominance of Classes 1 and 2 vegetation in Mrima Hill (Fig. 6) confirms that the area's laterite, which is rich in iron and manganese (Baker, 1953), contains high radioactive mineral content. This observation is supported by the gamma dose-rate measurements, which show that the measured dose-rates are highest at the hill peaks and southern hill slopes. The variation in vegetation species between Classes 1 and 2 could thus be attributed primarily to the area's underlying geological formations (see Fig. 2(b)). This is because the minerals and nutrients (taken up by the vegetation) that predominate in the soil are determined by the parent rock (Burghelea et al., 2015). The few pixels observed for Class 3 vegetation in the foot slopes of the hill could be indication that the species is fading away, perhaps due to human encroachment as the area lies outside the Mrima Hill forest reserve. In the Mrima hill environs, the distribution of the two classes of soil/rocks (Fig. 7) could be directly attributed to the soil and rock formations around the hill, namely sands and sandstones/shales/siltstones (see Fig. 2(b)). Class 1 soil/rocks (sandstones/shales/siltstones) therefore have higher radioactive mineral content compared to Class 2 soil/rocks (sands) which is consistent with observations made by Kaniu (2017).

The overall accuracy shows that 80% and 91% of all the pixels under assessment in Mrima Hill and the environs, respectively were correctly classified. On this basis, a projection of the air absorbed gamma dose-rates in areas where no radiometric measurements were previously taken but where spectral signatures of vegetation and soil/rocks were recorded is given (see Table 4). Furthermore, using the botanical method to assess spectral signatures of vegetation in the larger alkaline igneous complex of Jombo (Baker, 1953), it is shown in Fig. 8 that, in addition to Mrima Hill, Jombo Hill and Marenji forest have a high concentration of Class 1 and Class 2 vegetation species. This implies that the areas associated with these species are likely to contain radioactive minerals as well as high background radiation (i.e. >375 nGy h^{-1}), and that future mineral exploration and associated radiological monitoring activities would prioritize these areas.
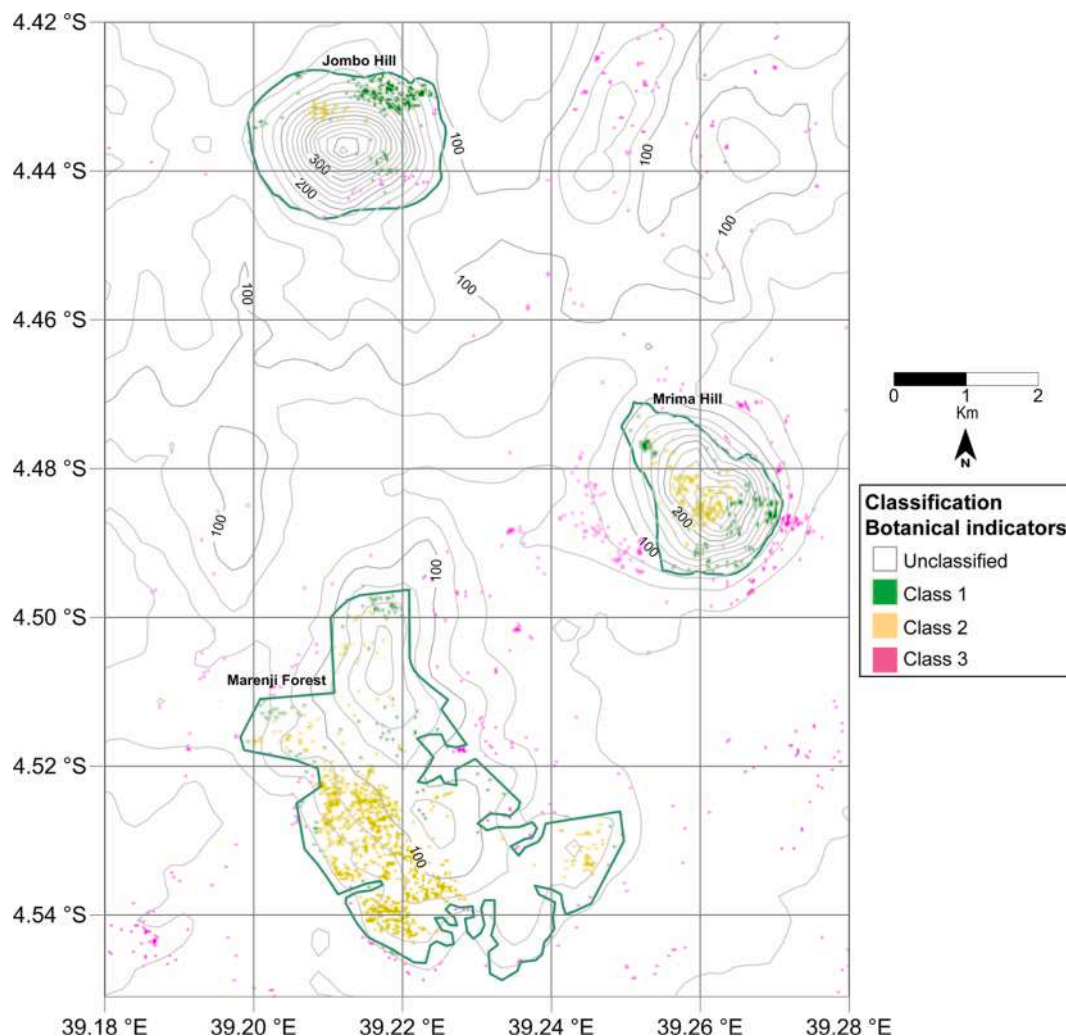

Fig. 8. Maximum likelihood classification of vegetation in the alkaline-igneous complex of Jombo that is associated with radioactive minerals.

5. Conclusion and recommendations

This study investigated the feasibility of using satellite data to identify and map radioactive minerals in an area with high background radiation levels, specifically Mrima Hill and its environs on Kenya's south coast. Image interpretation of Landsat 8 OLI datasets was used to identify spectral signatures of soil/rocks and vegetation associated with radioactive minerals. The maximum likelihood classification technique was found to be effective in mapping radioactive minerals after it was validated using air absorbed gamma dose-rate measurements in the area. Consequently, this method is recommended for mapping radioactive minerals and supporting environmental radiation measurements in high background radiation areas, particularly in remote areas with restricted access and resources. Use of high-resolution spectral and spatial remote sensing data is also recommended.

Declaration of Competing Interest

The authors declare that they have no known competing financial interests or personal relationships that could have appeared to influence the work reported in this paper.

Acknowledgements

References

Aage, H.K., Korsbech, U., Bargholz, K., Hovgaard, J., 2006. Carborne gamma-ray spectrometry. Calibr. Appl. 64, 948–956.

Abrams, M. and Yamaguchi, Y. (2019), Twenty years of ASTER contributions to lithologic mapping and mineral exploration, *Remote Sens.*, available at:10.3390/rs11111394.

Adelman-McCarthy, J.K., Agüeros, M.A., Allam, S.S., Anderson, K.S.J., Anderson, S.F., Annis, J., Bahcall, N.A., et al., 2006. The fourth data release of the sloan digital sky survey. Astrophys. J. Suppl. Ser. 162 (1), 38.

Amer, R., Kusky, T., El Mezayen, A., 2012. Remote sensing detection of gold related alteration zones in Um Rus area, Central Eastern Desert of Egypt. Adv. Sp. Res. 49 (1), 121–134.

Baker, B., 1953. The Alkaline Igneous Complex of Jombo, Nairobi.

Baranwal, V.C., Rønning, J.S., 2020. Airborne Geophysical Surveys and Their Integrated Interpretation, available at:10.1007/978-3-030-28909-6_14.

Boesche, N.K., Rogass, C., Lubitz, C., Brell, M., Herrmann, S., Mielke, C., Tonn, S., et al., 2015. Hyperspectral REE (rare earth element) mapping of outcrops-applications for neodymium detection. Remote Sens. 7 (5) https://doi.org/10.3390/rs70505160.

Burghelea, C., Zaharescu, D.G., Dontsova, K., Maier, R., Huxman, T., Chorover, J., 2015. Mineral nutrient mobilization by plants from rock: influence of rock type and arbuscular mycorrhiza. Biogeochemistry 124 (1-3), 187–203.

Chavez, P.S., 1996. Image-based atmospheric corrections-revisited and improved. Photogramm. Eng. Remote Sensing, [Falls Church, Va.] 62 (9), 1025–1035.

Crosta, A.P., De Souza Filho, C.R., Azevedo, F., Brodie, C., 2003. Targeting key alteration minerals in epithermal deposits in Patagonia, Argentina, using ASTER imagery and principal component analysis. Int. J. Remote Sens. 24 (21), 4233–4240.

Crowley, J.K., Brickey, D.W., Rowan, L.C., 1989. Airborne imaging spectrometer data of the Ruby Mountains, Montana: Mineral discrimination using relative absorption band-depth images. Remote Sens. Environ. 29 (2), 121–134.

Dev Acharya, T., Yang, I., Student, G., 2015. Exploring Landsat 8 Urban Landcover and Their Change in Nepal View Project Geographic Information Systems for Transportation (GIS-T) in Nepal View Project Exploring Landsat 8. Int. J. IT, Eng. Appl. Sci. Res. 4.

Gillman, C., 1949. A vegetation-types map of Tanganyika Territory. Geogr. Rev., JSTOR 39 (1), 7–37.

JICA, 1993. Report on the Mineral Exploration in the Mombasa Area Republic of Kenya: Phase III.

Kaniu, M.I., 2017. In-Situ Gamma-Ray Spectrometry and Associated Radiometric Assessment of the Mrima-Kiruku Complex (Kenya) High Background Radiation Anomaly. University of Nairobi.

Kaniu, M.I., Angeyo, H.K., Darby, I.G., Muia, L.M., 2018a. Rapid in-situ radiometric assessment of the Mrima-Kiruku high background radiation anomaly complex of Kenya,. J. Environ. Radioact. 188, 47–57.

Kaniu, M.I., Angeyo, K.H., Darby, I.G., 2018b. Occurrence and multivariate exploratory analysis of the natural radioactivity anomaly in the south coastal region of Kenya. Radiat. Phys. Chem. 146 https://doi.org/10.1016/j.radphyschem.2018.01.009.

Kaniu, M.I., Darby, I.G., Angeyo, H.K., 2019. Assessment and mapping of the high background radiation anomaly associated with laterite utilization in the south coastal region of Kenya. J. African Earth Sci. 160, 103606. https://doi.org/10.1016/j.jafrearsci.2019.103606.

Killeen, P.G., Mwenifumbo, C.J., Ford, K.L., 2015. Tools and Techniques: Radiometric Methods, Treatise Geophys., second Ed., vol. 11, Elsevier Inc., pp. 447–524.

Leverington, D.W., Moon, W.M., 2012. Landsat-TM-based discrimination of lithological units associated with the Purtuniq ophiolite, Quebec, Canada, Remote Sens., vol. 4 (5), available at: 10.3390/rs4051208.

Lillesand, T., Kiefer, R., Chipman, J., 2015. Remote Sensing and Image Interpretation, seventh Ed. John Wiley Sons Inc, New York.

Manuel, R., Brito, M. da G., Chichorro, M., Rosa, C., 2017. Remote sensing for mineral exploration in central Portugal. Minerals 7 (10). https://doi.org/10.3390/min7100184.

Mather, P.M., Koch, M., 2010. Computer Processing of Remotely-Sensed Images: An Introduction, Fourth Edition, Comput. Process. Remote. Images An Introd, fourth ed., available at:10.1002/9780470666517.

Mohamed, M.T.A., Al-Naimi, L.S., Mgbeojedo, T.I., Agoha, C.C., 2021. Geological mapping and mineral prospectivity using remote sensing and GIS in parts of Hamissana, Northeast Sudan. J. Pet. Explor. Prod. 11 (3), 1123–1138.

Muavhi, N., Mavhungu, M.E., Ndivhudzannyi, R., 2021. Mapping of potential rare earth deposits in the Schiel alkaline complex using sentinel-2B multispectral sensor. Egypt. J. Remote Sens. Sp. Sci. https://doi.org/10.1016/j.ejrs.2021.05.002.

Neave, D.A., Black, M., Riley, T.R., Gibson, S.A., Ferrier, G., Wall, F., Broom-Fendley, S., 2016. On the feasibility of imaging carbonatite-hosted rare earth element deposits using remote sensing. Econ. Geol. 111 (3) https://doi.org/10.2113/econgeo.111.3.641.

Pacheco, A., McNairn, H., 2010. Evaluating multispectral remote sensing and spectral unmixing analysis for crop residue mapping. Remote Sens. Environ. 114 (10) https://doi.org/10.1016/j.rse.2010.04.024.

Rajan Girija, R., Mayappan, S., 2019. Mapping of mineral resources and lithological units: a review of remote sensing techniques. Int. J. Image Data Fusion. https://doi.org/10.1080/19479832.2019.1589585.

Rajesh, H.M., 2004. Application of remote sensing and GIS in mineral: Resource mapping - An overview. J. Mineral. Petrol. Sci. 99 (3), 83–103.

Ramadan, T.M., Ibrahim, T.M., Said, A.D., Baiumi, M., 2013. Application of remote sensing in exploration for uranium mineralization in Gabal El Sela area, South Eastern Desert, Egypt. Egypt. J. Remote Sens. Sp. Sci. 16 (2), 199–210.

Ramadan, T.M., El Leithy, B.S., 2005. Application of airborne radiometric data and Landsat TM imagery in exploration for the mineralization in El Qasia-Umm Naggat granites, Central Eastern Desert, Egypt. Egypt. J. Remote Sens. Sp. Sci. 8, 143–160.

Rokos, D., Argialas, D., Mavrantza, R., Seymour, K.S., Vamvoukakis, C., Kouli, M., Lamera, S., et al., 2000. Structural analysis for gold mineralization using remote sensing and geochemical techniques in a GIS environment: island of Lesvos, Hellas. Nat. Resour. Res. 9 (4), 277–293.

Rowan, L.C., Mars, J.C., 2003. Lithologic mapping in the Mountain Pass, California area using Advanced Spaceborne Thermal Emission and Reflection Radiometer (ASTER) data. Remote Sens. Environ. 84 (3), 350–366.

Sabins, F.F., 1999. Remote sensing for mineral exploration. Ore Geol Rev. 14 (3–4), 157–183.

Samanga, R., 2021. Remote-Sensing Applications for Mineral Mapping: Boosting Zimbabwe's Foreign Direct Investment Potential Through Sustainable Technology, available at:10.1007/978-3-030-59158-8_2.

Shi, X., Al-Arifi, N., Abdelkareem, M., Abdalla, F., 2020. Application of remote sensing and GIS techniques for exploring potential areas of hydrothermal mineralization in the central Eastern Desert of Egypt. J. Taibah Univ. Sci. 14 (1), 1421–1432.

Sleumer, H., Polhill, R.M., Beentje, H.J., 1975. Flora of Tropical East Africa. Crown Agents for the Colonies.

Song, C., Woodcock, C.E., 2003. Monitoring forest succession with multitemporal Landsat images: Factors of uncertainty. IEEE Trans. Geosci. Remote Sens., IEEE 41 (11), 2557–2567.

Thomas, M.D., Ford, K.L., Keating, P., 2016. Review paper: Exploration geophysics for intrusion-hosted rare metals. Geophys. Prospect. 64 (5) https://doi.org/10.1111/1365-2478.12352.

Turner, D.J., Rivard, B., Groat, L.A., 2014. Visible and short-wave infrared reflectance spectroscopy of REE fluorocarbonates. Am. Mineral. 99 (7) https://doi.org/10.2138/am.2014.4674.

UNSCEAR, 2000. Sources and Effects of Ionizing Radiation, ANNEX B, Exposures from Natural Radiation Sources, New York.

Verplanck, P.L., Gosen, B.S.V., 2011. Carbonatite and Alkaline Intrusion-Related Rare Earth Element Deposits — A Deposit Model. Surv. U S Geol. 1–8.

Yang, C., Lu, L., Lin, H., Guan, R., Shi, X., Liang, Y., 2008. A fuzzy-statistics-based principal component analysis (FS-PCA) method for multispectral image enhancement and display. IEEE Trans. Geosci. Remote Sens. 46 (11) https://doi.org/10.1109/TGRS.2008.2001386.

Yu, L., Porwal, A., Holden, E.J., Dentith, M.C., 2011. Suppression of vegetation in multispectral remote sensing images. Int. J. Remote Sens. 32 (22) https://doi.org/10.1080/01431161.2010.523726.